

Chapter 2

Electronic Properties of III-V Quantum Dots

Andrei Schliwa, Gerald Hönig, and Dieter Bimberg

Abstract Electronic properties of quantum dots are reviewed based on eight-band **k-p** theory. We will focus on the following interrelated subjects: First the role of crystallographic symmetry is evaluated. This includes the symmetry of the lattice of the substrate [wurtzite (wz) versus zinc blende (zb)] as well as different substrate orientations [zb-(001) versus zb-(111)]. Second, we discuss two different types of band alignment, type-I versus type-II, by comparing the common-anion system zb-InAs/GaAs to the common-cation system zb-GaSb/GaAs. Finally, the impact of large built-in fields resulting from piezo- and pyroelectric charges will be exemplified for the wz-GaN/AlN QD-system.

2.1 Introduction

Semiconductor quantum dots (QD) are fascinating physical subjects exhibiting electronic properties even simpler than hydrogen but in a dielectric cage, thus merging semiconductor with atomic physics. Nano-structures based on III-V-system material combinations alone cover a huge range of very different electronic and optical properties. Their tremendous tunability will be exemplified in this contribution by focusing on three cornerstones of current research: (i) InAs/GaAs-, (ii) GaAs/GaSb-, and (iii) GaN/AlN quantum dots.

- (i) InAs/GaAs QDs have been subject of intense research for the last 20 years [13, 29], which led—most prominently—to the development of quantum dot

A. Schliwa (✉) • G. Hönig • D. Bimberg
Institut für Festkörperphysik, Technische Universität Berlin, Hardenbergstr. 36, 10623
Berlin, Germany
e-mail: andrei.schliwa@gmail.com; gerald.hoenig@physik.tu-berlin.de;
bimberg@physik.tu-berlin.de

lasers [40] and single-photon emitters [48]. As InAs is a small band-gap material, including coupling between valence- and conduction bands became essential for the predictive power of any electronic structure calculations. This demand led to the development of 3D QD models going beyond effective mass theory [35]. Most transparent are calculations based on eight-band **k·p** theory [74]. Triggered by the quest for single and entangled photon emitters, later on, the role of substrate orientation went into the focus of research [65, 71] which will be one topic of this chapter.

- (ii) While the InAs/GaAs system exhibits a type-I quantum confinement, where both electron *and* hole are localized in the QD, GaSb/GaAs quantum dots feature a type-II band-alignment: The confinement is attractive alone for holes but repulsive for electrons. If holes are stored in the QD, eventually the band structure is modified to allow electrons to be localized nearby at the interface by means of Coulomb interaction. The difference between the two material combinations with respect to band-alignment can be traced back to the fact that InAs/GaAs share a common-anion- and GaSb/GaAs a common cation, as will be further elaborated in Sect. 2.3.2.
- (iii) The third material system of huge interest is GaN/AlN. The difference to the former two is threefold: First, state-of-the-art QDs are synthesized in the wurtzite phase, as opposed to the zinc blende lattice of the preceding systems. Second, GaN has a large band gap and, third, the system GaN/AlN exhibits very strong internal piezo- and pyroelectric fields. We will see in Sect. 2.3.3 that for GaN/AlN QDs simply by variation of the QD size a large (interband) photon emission tunability ranging from 2.6 to 4.5 eV is obtained.

All three heterostructures belong to the III-V material system and coherent growth is mediated by the sufficiently large lattice mismatch leading to QD formation in the Stranski-Krastanov growth mode [68]. Strain alone already imposes significant band-shifts and band-splittings (heavy-hole/light-hole). Moreover, the lack of inversion symmetry in all III-V systems together with the inhomogeneity of the strain give rise to additional piezoelectric built-in fields.

The appeal of eight-band **k·p** theory lies in the attractive balance between accuracy, speed of computation, and transparency of the physics and the parameters used. All relevant phenomena, such as confinement, strain, piezo- and pyroelectricity, band-coupling and -splitting can be reliably treated for any shape, size and composition as long as the involved materials feature a direct band gap. This opens the opportunity to employ the model for the purpose of inverse bandstructure modeling [64] and inverse design [51].

2.1.1 Role of Lattice Symmetries (Zinc Blende vs Wurtzite)

The majority of quantum dots either carry zinc blende or wurtzite symmetry. Sometimes—as in the case of GaN—both allotropes are proven to exist. The zinc

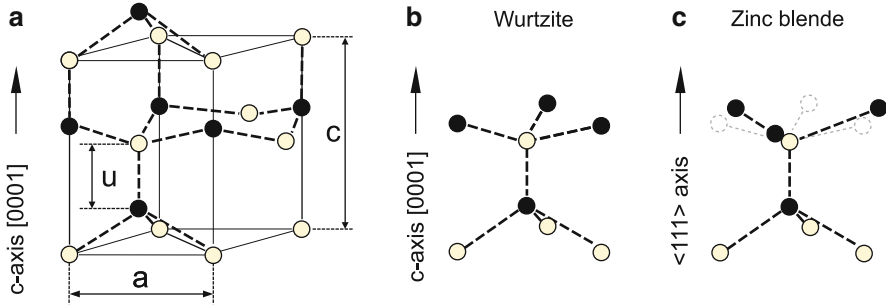


Fig. 2.1 (a) Wurtzite unit cell with lattice parameters a and c together with the internal parameter u . (b and c) The differences in position of second nearest neighbours between wurtzite and zinc blende lattice are shown

blende and wurtzite lattice differ only in the second-nearest neighbours [see Fig. 2.1b,c]. Analogous to the hexagonal and cubic close packing one can describe them by different layer sequences $ABABAB$ (along c -axis) or $ABCABCA$ (along $\langle 111 \rangle$ -axis).

These minute differences however result in very different symmetry properties: the zinc blende crystal has four threefold axes of rotation ($\langle 111 \rangle$) and, thus, a higher symmetry than the wurtzite lattice with only one axis with threefold rotational symmetry (c -axis = $[0001]$). The latter gives rise to two important peculiarities: (1) the emergence of spontaneous polarization resulting in the pyroelectric effect (often used synonymously), and as a consequence (2) the crystal field splitting leading to a splitting of heavy and light hole (also referred to as A and B bands).

Whereas the zinc blende unit cell is sufficiently described by one lattice constant, a , for the wurtzite unit cell two lattice constants, a and c , together with an internal parameter u are required to adequately describe the lattice structure (see Fig. 2.1). The structure is composed of two interpenetrating hexagonal closed package sublattices. For the ideal wurtzite unit cell the ratio of c and a is $c/a = \sqrt{8/3} = 1.633$ and the internal parameter u has a value of $u = 3/8 = 0.375$ in fractional coordinates. The lattice is composed of tetrahedra with four atoms of one species tetrahedrally coordinated around a central atom of the other species. In case of an ideal ratio of lattice constants and ideal internal parameter the bond length and the bond angles between the nearest neighbors are equal, but the distance to the second nearest neighbor along the c -axis is about 13 % shorter than the distance to the other second nearest neighbors [2]. Hence, as was calculated by Bernardini et al. [9] already in this ideal case a spontaneous polarization arises.

GaN departs only little from the ideal situation with a $(c/a)_{\text{GaN}} = 1.627$ and $u_{\text{GaN}} = 0.377$, whereas AlN shows more significant deviations with $(c/a)_{\text{AlN}} = 1.601$ and $u_{\text{AlN}} = 0.382$, which correlates with the difference between the electronegativities of the two constituents [9].

The situation is schematically depicted in Fig. 2.2. One important consequence is the non-ideality of the tetrahedra as shown in Fig. 2.2b which amplifies the

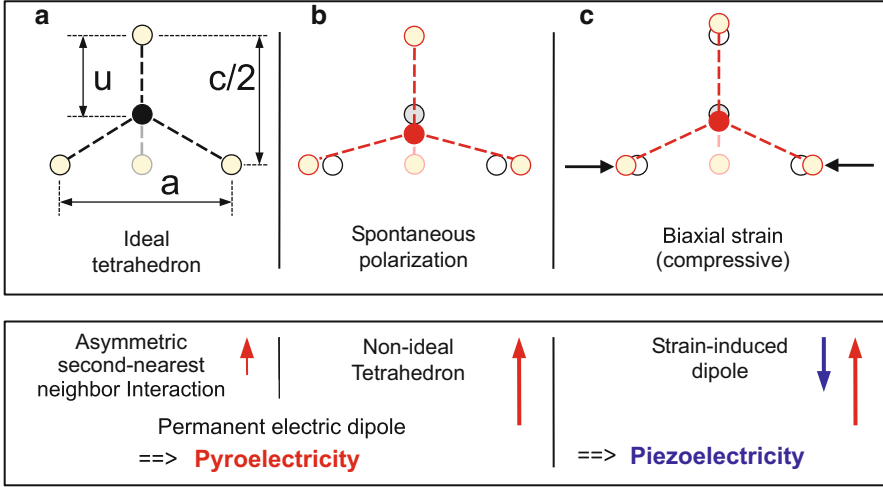


Fig. 2.2 (a) Ideal and (b,c) non-ideal tetrahedra. Due to asymmetric second-nearest neighbor interaction, already in the case of an ideal tetrahedron, differences in electronegativity between cation and anion lead to spontaneous polarization [3,9]. (b) The pyroelectric effect is enhanced by the spontaneous polarization causing a non-ideal tetrahedron. (c) Strain (here biaxially compressive) leads to piezoelectricity

(pyroelectric) polarization of the lattice. For heterostructures such as wz-GaN/AlN differences between the spontaneous polarization fields ($P_{sp}^{AlN} = -0.09 \text{ C/m}^2$ compared to $P_{sp}^{GaN} = -0.034 \text{ C/m}^2$) result in large residual charges at the heterointerface being the root for the large built-in fields in GaN/AlN heterostructures.

Because the lattice mismatch between AlN and GaN is about 2.5 %, coherent growth leads to strain and, hence, to an additional piezoelectric field superimposed to the pyroelectric field as depicted in Fig. 2.2c.

In zinc blende crystals, in particular for the zb-III-V system, the piezoelectric effect is much smaller than for wz-III-nitride material. Nevertheless, it breaks the confinement symmetry even in circular symmetric quantum dots, and presents one important factor for the excitonic fine-structure splitting. The mechanism, how shear strain causes a piezoelectric polarization is schematically shown in Fig. 2.3.

2.2 Method of Calculation

Figure 2.4 shows schematically the modeling procedure employed in this work. It starts with an implementation of the 3D QD model structure (size, shape, chemical composition), and continues with the calculation of strain, piezoelectricity, and pyroelectricity (wurtzite only). The resulting strain and polarization fields enter the eight-band $\mathbf{k} \cdot \mathbf{p}$ Hamiltonian. Solution of the Schrödinger equation yields

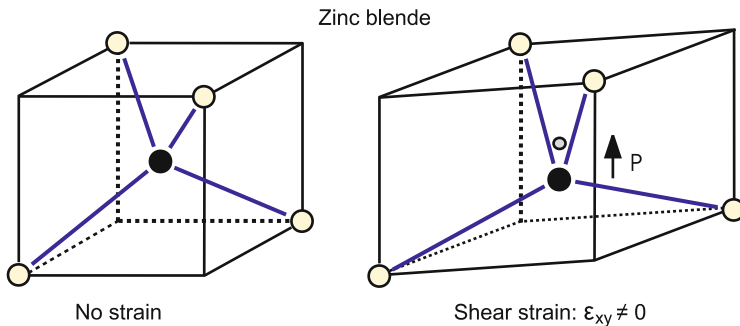


Fig. 2.3 Part of the zinc blende unit cell in absence of strain (*left*) and presence of one shear strain component, $\epsilon_{xy} \neq 0$ (*right*): Cations and anions do not share the same center of charge anymore, which results in a piezoelectric dipole

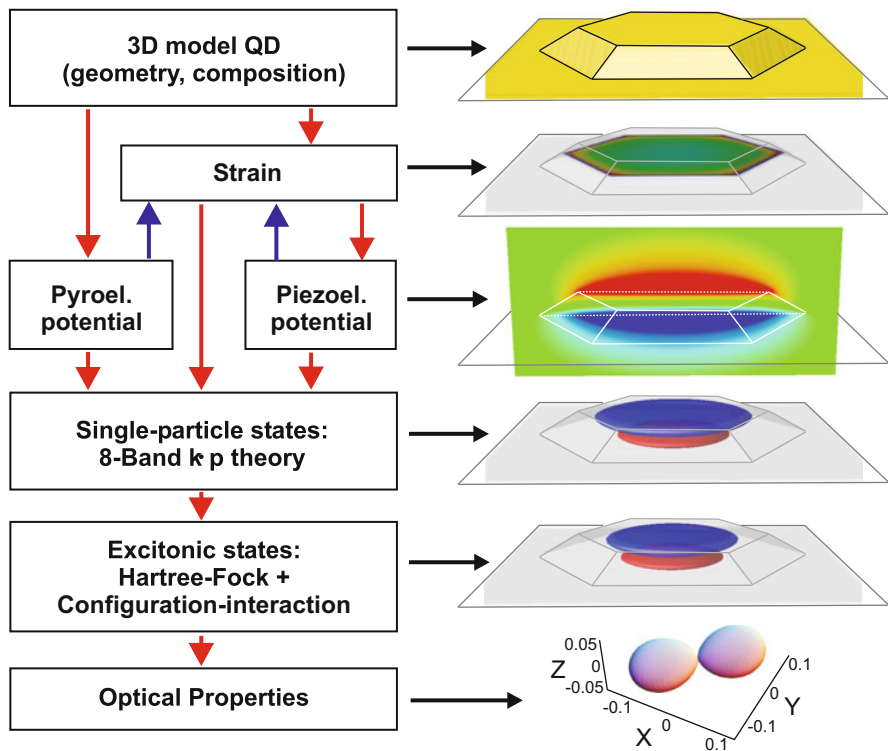


Fig. 2.4 Schematics of the modeling procedure applied in this work

electron and hole single-particle states. Coulomb interaction is accounted for by employing the configuration interaction method based either on the pristine single-particle states or on Hartree-Fock modified states. Finally, optical properties such as absorption spectra, capture cross sections or lifetimes can be calculated.

2.2.1 Calculation of Strain

Since the impact of strain on the confinement is comparable to that of the band offset resulting from the variation of the chemical composition at the heterojunctions, the wavefunctions and energies strongly depend on the underlying strain distribution. The impact of our model used for calculating the strain distribution has been analysed in a number of publications [55, 74]. Stier et al. [74] argue that the continuum elasticity model (CM) gives better results for QDs than the valence force field (VFF) model (Keating) in its linearized version (Kane). The major part of the differences in the strain distribution are attributed to the incorrect value of C_{44} in the VFF model and not to its atomistic character. Later Zunger et al. [80] introduced a generalized version of the VFF model—the G-VFF model—where C_{44} is incorporated correctly. Although the potential of the Keating model in its original version is not harmonic, it has been remarked by Kane [38], that anharmonic effects due to higher order terms are not satisfactorily treated. Therefore Klimeck and coworkers extended this model to include them correctly [42]. The same issue is addressed by Hammerschmidt et al. [30] and Migliorato et al. [49] who employed the Tersoff-potential method [76].

The choice of the most appropriate strain model depends on the choice of the model for the electronic structure calculations. Since the eight-band $\mathbf{k}\cdot\mathbf{p}$ model presents a continuum approach, an atomistic strain model cannot unfold its full potential for two reasons:

First, the mapping of the atomic positions onto a strain tensor field is associated with a loss of information. To describe the positions of four tetrahedrally coordinated In atoms around an As atom five times the three spatial dimensions = 15 parameters are required. The strain tensor field on the other hand is described by only six independent components at each local position.

Second, the $\mathbf{k}\cdot\mathbf{p}$ model provides only a limited number of parameters to account for the strain, the model is not sensitive to the complete information an atomistic model provides. For example for a QD having a fourfold rotational C_{4v} symmetry the strain tensor derived from the CM model has C_{4v} symmetry too. The tetrahedral configuration of the atoms in the atomistic models in contrast [55] leads to C_{2v} symmetry, i.e. the strain components are different along the $[110]$ and $[1\bar{1}0]$ directions and the p -states will split. In our approach a structural $C_{\infty v}$ or C_{4v} symmetry is reduced in the second step by the inclusion of the piezoelectric field.

2.2.2 Piezoelectricity/Pyroelectricity

2.2.2.1 Zinc Blende Crystal

Piezoelectricity is defined as the generation of electric polarization by application of stress to a crystal lacking a center of symmetry [1]. The zinc blende structure is the

simplest example of such a lattice and the strength of the resulting polarization is described by one parameter alone, e_{14} , alone for the linear case and three parameters, B_{114} , B_{124} and B_{156} for the quadratic case [10] resulting in

$$\begin{aligned}
 \mathbf{P}_1 &= 2 e_{14} \begin{pmatrix} \epsilon_{yz} \\ \epsilon_{xz} \\ \epsilon_{xy} \end{pmatrix} , \\
 \mathbf{P}_2 &= 2 B_{114} \begin{pmatrix} \epsilon_{xx} \epsilon_{yz} \\ \epsilon_{yy} \epsilon_{xz} \\ \epsilon_{zz} \epsilon_{xy} \end{pmatrix} + \\
 &+ 2 B_{124} \begin{pmatrix} \epsilon_{yz} (\epsilon_{yy} + \epsilon_{zz}) \\ \epsilon_{xz} (\epsilon_{zz} + \epsilon_{xx}) \\ \epsilon_{xy} (\epsilon_{xx} + \epsilon_{yy}) \end{pmatrix} + \\
 &+ 4 B_{156} \begin{pmatrix} \epsilon_{xz} \epsilon_{xy} \\ \epsilon_{yz} \epsilon_{xy} \\ \epsilon_{yz} \epsilon_{xz} \end{pmatrix} .
 \end{aligned} \tag{2.1}$$

The resulting polarization \mathbf{P}_{zb} then comprises of two components

$$\mathbf{P}_{zb} = \mathbf{P}_1 + \mathbf{P}_2 .$$

2.2.2.2 Wurtzite Crystal

The total polarization \mathbf{P}_{wz} in wurtzite-type semiconductors is given by

$$\mathbf{P}_{wz} = \mathbf{P}_{\text{spont}} + \mathbf{P}_{\text{piezo}} ,$$

where $\mathbf{P}_{\text{piezo}}$ is the strain-induced piezoelectric polarization and $\mathbf{P}_{\text{spont}}$ the spontaneous polarization.

Due to the reduced symmetry of the wurtzite lattice three parameters, e_{15} , e_{31} and e_{33} are required to capture the piezoelectric polarization, resulting in

$$\mathbf{P}_{\text{piezo}} = \begin{pmatrix} 2 e_{15} \epsilon_{xz} \\ 2 e_{15} \epsilon_{yz} \\ e_{31} \epsilon_{xx} + e_{31} \epsilon_{yy} + e_{33} \epsilon_{zz} \end{pmatrix} .$$

The spontaneous polarization $\mathbf{P}_{\text{spont}}$ is given by

$$\mathbf{P}_{\text{spont}} = \begin{pmatrix} 0 \\ 0 \\ P_{\text{spont}} \end{pmatrix} .$$

2.2.2.3 Built-in Potential

The polarization fields \mathbf{P}_{zb} for the zinc blende crystal or \mathbf{P}_{wz} for the wurtzite crystal, respectively, induce a charge distribution ρ_p :

$$\rho_p(\mathbf{r}) = -\nabla \cdot \mathbf{P}_{\text{zb/wz}} \quad .$$

The resulting built-in potential is obtained by solving Poisson's equation, taking into account the material dependent static dielectric constants $\epsilon_s(\mathbf{r})$

$$\rho_p(\mathbf{r}) = \epsilon_0 \nabla \cdot \{ \epsilon_s(\mathbf{r}) \nabla V_p(\mathbf{r}) \} \quad , \quad (2.2)$$

\Leftrightarrow

$$\Delta V_p(\mathbf{r}) = \frac{\rho_p}{\epsilon_0 \epsilon_s(\mathbf{r})} - \frac{1}{\epsilon_s(\mathbf{r})} \nabla V_p(\mathbf{r}) \cdot \nabla \epsilon_s(\mathbf{r}) \quad . \quad (2.3)$$

The first term on the right hand side of Eq. 2.3 refers to the true three-dimensional charge density while the second is the contribution of polarization interface charge densities due to a discontinuous $\epsilon_s(\mathbf{r})$ across heterointerfaces.

The importance of the second order term \mathbf{P}_2 for InGaAs/GaAs(111) quantum wells (QW) and QDs has been pointed out by Bester et al. [10]. They found that for QWs the linear and quadratic coefficients have opposite effects on the field, and for large strain the quadratic term even dominates. For InAs/GaAs QDs, however, the situation is more complex since in addition to the large strain their three-dimensional structure comes into play: The linear term generates a quadrupole-like potential which reduces a structural C_{4v} - or $C_{\infty v}$ -symmetry of a QD to C_{2v} [11, 29]. The effect of the quadratic terms has been evaluated recently by Bester et al. [12] for lens-shaped QDs and was found to cancel the first order potential inside the QD leading to a field free QD. The investigation was later extended to a variety of more realistic structures including truncated pyramids, and non-evenly alloyed QDs [63]. For a pyramidal model QD having a base length of 17 nm and $\{101\}$ side facets the strength and distribution of the piezoelectric potential resulting from the two orders of the piezoelectric tensor are displayed in Fig. 2.5. Apart from the different orientation and sign of the two contributions, an important peculiarity of the second order potential is its restriction to the interior of the QD which is in apparent contrast to the widely extended first order field. The difference is linked to the origin of the polarization \mathbf{P} : \mathbf{P}_1 is a function of the shear-strain components alone, whereas \mathbf{P}_2 results mainly from the product of the diagonal and the shear-strain. However, in contrast to the shear-strain components, the diagonal elements ϵ_{ii} are large only inside the QD and its close vicinity and therefore \mathbf{P}_2 -charges can only be created in this region.

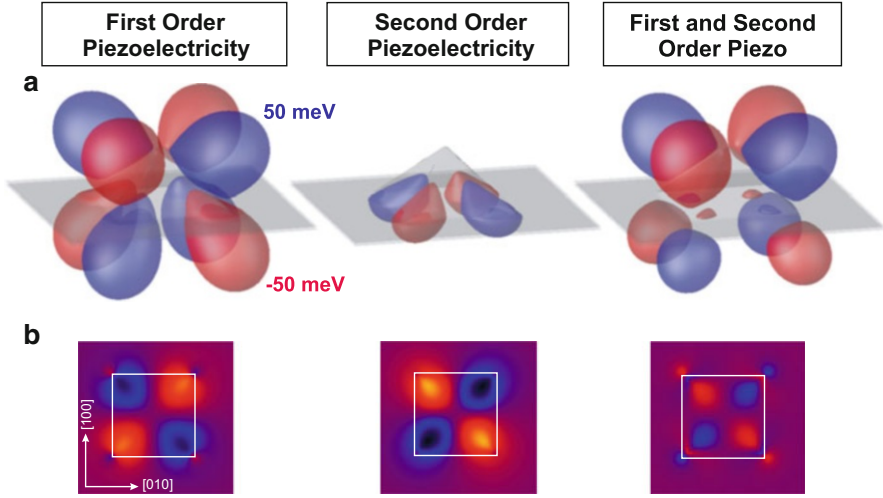


Fig. 2.5 (a) The piezoelectric potential isosurfaces at ± 50 meV of a pyramidal InAs quantum dot with 17 nm base length shown for the linear, the quadratic part and for both. (b) Contour plots of the piezoelectric potential 2 nm above the wetting layer. (see [63])

2.2.3 Eight-Band $\mathbf{k}\cdot\mathbf{p}$ Method: Single Particle States

The energy levels and wavefunctions of bound electron and hole states are calculated using the eight-band $\mathbf{k}\cdot\mathbf{p}$ model. The theory was originally developed for the description of electronic states in bulk material [23, 37, 52]. For the use in heterostructures the envelope function version of the model has been developed and applied to quantum wells [27], quantum wires [73] and quantum dots [35, 44, 54, 74]. Details of the principles of our implementation for zinc blende heterostructures are outlined in [73].

This model enables us to treat QDs of arbitrary shape and material composition, including the effect of strain, piezoelectricity, VB mixing and CB-VB interaction. The strain enters our model via the use of deformation potentials as outlined by Bahder [8]. Its impact on the local band edges as a function of the QD geometry will be discussed in the next sections.

The $\mathbf{k}\cdot\mathbf{p}$ model, when applied to small quantum structures, has in principle a few well-known drawbacks which have been examined in detail in [25, 39]. They are basically related to the fixed number of Bloch functions used for the wavefunction expansion, the restriction to the close vicinity of the Brillouin zone center Γ and to the limited ability to account for the symmetry of the underlying lattice. These problems do not arise in microscopic theories like the empirical pseudopotential [39] (EPM) or the empirical tight-binding method [43, 61] (ETB), which a priori have greater potential of accuracy. This potential, however, can only be exploited if the corresponding input parameters—the form factors in the

EPM or the tight-binding parameter and their strain dependence in the ETB—are known with sufficient accuracy. Reliable generation of these parameters, however, is highly nontrivial and yet at least controversial if not unsolved. One of the most appealing features of the **k**·**p** model, in contrast, is the direct availability of all the parameters entering the calculations and the corresponding transparency of the method. Additionally, the required computational expense of the method is comparatively small.

k·**p** models for wurtzite nitride QDs have been presented before, most prominent by Andreev and O'Reilly [4] and Fonoberov and Balandin [24]. The differences between these two models and the model used in the present work have been discussed in [81] and shall be summarized briefly here:

- (i) The method introduced by Andreev and O'Reilly [4] includes all important effects except spin-orbit splitting, which has been neglected in order to reduce the dimensions of the Hamiltonian from 8×8 to 4×4 . This simplification can be justified, given that the spin-orbit splitting is small in GaN (17 meV) and AlN (19 meV) and modifies the absolute value of the exciton transition energies roughly by the same amount. InN shows an even smaller spin-orbit splitting of 5 meV [77]. However, neglecting spin-orbit splitting leads to an artificial degeneracies in the hole spectra, in particular of the hole ground states [81].
- (ii) Fonoberov and Balandin [24] use a 6×6 Hamiltonian for the valence bands (VBs), and the effective mass approximation for the conduction band (CB). This method neglects the coupling between VBs and CB, which is justified for large band-gap materials such as GaN and AlN. InN, in contrast, has a much smaller band gap of ≈ 0.7 meV and therefore requires the inclusion of VB/CB-coupling.

Meanwhile, also a full-fledged eight-band **k**·**p** implementation for wurtzite and zinc blende QDs is (freely) available within the *nextnano*³ project. Calculations for group-III-nitride QDs using the atomistic tight-binding model [72] have been presented for InGaN/GaN-QDs [59], GaN/AlN-QDs [56], and recently for pure InN/GaN-QDs [6, 7]. An in-depth comparative discussion is beyond the scope of the work.

2.2.4 Impact of Strain on Bulk Band Structure

In the context of heterostructures it is important to use a method for electronic structure calculations that fits the following requirements:

- Sensitivity for inhomogeneous strain. This covers band shifts due to hydrostatic strain, valence-band splitting arising from biaxial strain, and a strain-dependent conduction-band curvature or in other words: a strain-dependent effective electron mass.

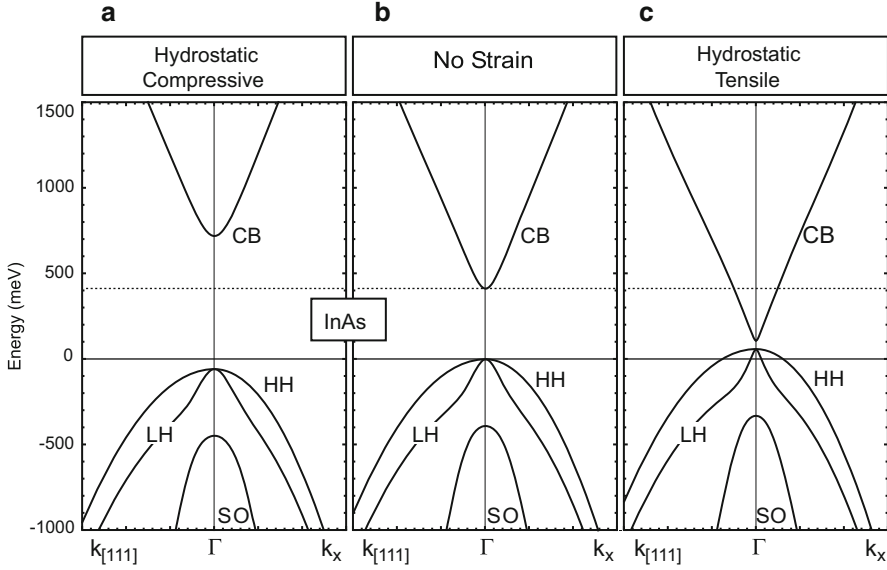


Fig. 2.6 Eight-band $\mathbf{k}\cdot\mathbf{p}$ bandstructure for InAs in presence of hydrostatic strain, $\epsilon_{xx} = \epsilon_{yy} = \epsilon_{zz}$: (a) Compressive hydrostatic strain, $\epsilon_H < 0$, and (c) tensile hydrostatic strain, $\epsilon_H > 0$. Case (b) refers to the absence of any strain

- Non-parabolicity effects. The Fourier-transform of a localized envelope functions spans a certain region in the vicinity of the Γ -point in the Brillouin-zone. Hence, to avoid overconfinement effects, the non-parabolic nature of the conduction band needs to be accounted for.

In the following section we will see, how eight-band $\mathbf{k}\cdot\mathbf{p}$ theory meets the outlined demands.

2.2.4.1 Zinc Blende Structure

Figure 2.6b shows the eight-band $\mathbf{k}\cdot\mathbf{p}$ bandstructure of bulk-InAs in absence of strain. Heavy hole (HH) and light hole (LH) bands are degenerate at the Γ -point, the split-off (SO) well separated due to spin-orbit interaction. The conduction band is *not parabolic* due to the conduction-band valence-band coupling mediated by the $\mathbf{k}\cdot\mathbf{p}$ term. This effectively decreases the electron effective mass of a localized electron state.

The impact of hydrostatic strain ($\epsilon_H = \epsilon_{xx} + \epsilon_{yy} + \epsilon_{zz}$) is shown in Fig. 2.6a, c. Compressive strain shifts the conduction band up, thus, increasing the band gap. Tensile strain on the other hand decreases the band gap.

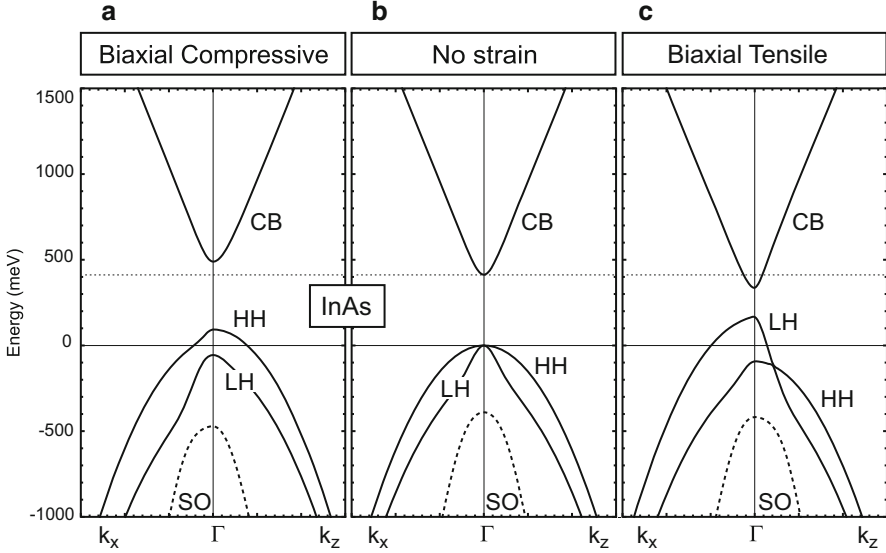


Fig. 2.7 Eight-band $\mathbf{k}\cdot\mathbf{p}$ bandstructure for InAs in presence of (a) biaxial compressive strain, with $\epsilon_{xx} = \epsilon_{yy} < 0$ and, $\epsilon_{zz} > 0$, (c) biaxial tensile strain, with $\epsilon_{xx} = \epsilon_{yy} > 0$ and, $\epsilon_{zz} < 0$. Case (b) refers to the absence of any strain. Material parameters are taken from [74]

If the main diagonal strain components are not the same, biaxial strain arises, as known from the classic case of strained quantum wells. These cases are considered in Fig. 2.7: Biaxial compressive strain (Fig. 2.7a) refers to $\epsilon_{xx} = \epsilon_{yy} < 0$ and, as a consequence of the Poisson effect, $\epsilon_{zz} > 0$, leads primarily to a splitting of the valence bands into a top lying HH- and a lower energy LH band. Note that the curvature of the HH band is ‘heavier’ in k_z -direction, which would be the confinement direction in case of a quantum well. Biaxial tensile strain (Fig. 2.7c) reverses the HH-LH ordering at the Brillouin-center.

Strain Dependent Electron Effective Mass

Cusack and coworker [21] were the first to point at the importance of the strain dependence of the electron effective mass in the context of strained quantum dots. The consequences for compressively strained QDs are smaller electron confinement energies as well as a decreased electron sub-level spacing.

This effect is accounted for in eight-band $\mathbf{k}\cdot\mathbf{p}$ theory: The hydrostatic strain strongly affects the band gap energy. As the strength of the $\mathbf{k}\cdot\mathbf{p}$ matrix elements critically depends on the band gap, the conduction band curvature and, hence, the electron effective mass is strongly modified by strain. This is depicted in Fig. 2.8. For tensile strain (Fig. 2.8a) the CB-curvature near the Γ -point increases, which

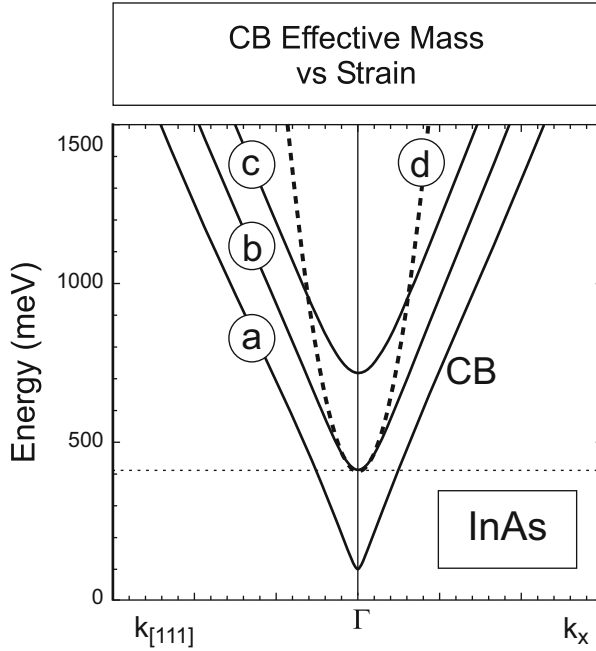


Fig. 2.8 Curvature of the conduction band as function of hydrostatic strain: (a) tensile strain, (b) no strain, (c) compressive strain. In case (d) no CB-VB coupling is present

translates into a lighter electron effective mass. For compressive strain (Fig. 2.8c), which corresponds to the case of InAs/GaAs quantum dots, on the other hand, the electron becomes heavier than in absence of strain. The impact of $\mathbf{k} \cdot \mathbf{p}$ coupling can be seen by comparing the curves Fig. 2.8(b and c), where in case (d) the coupling is switched off.

2.2.4.2 Wurtzite Structure

There are two major differences between the zb-InAs/GaAs system and the wz-GaN/AlN.

The first one is related to the much smaller band gap of InAs compared to GaN, which leads to a stronger CB-VB coupling for InAs. The small effect of CB-VB coupling in the GaN system is visible in Fig. 2.9a when comparing case (ii), which includes CB-VB coupling, and case (iv), where the coupling is switched off: the coupling induces no significant change of the CB-curvature near the Γ -point.

The second difference refers to the crystal-field splitting as a consequence of the spontaneous polarization present in the wz-GaN system: even if no strain is present, HH-hole and LH-hole are not degenerate at the zone-center anymore (Fig. 2.9b).

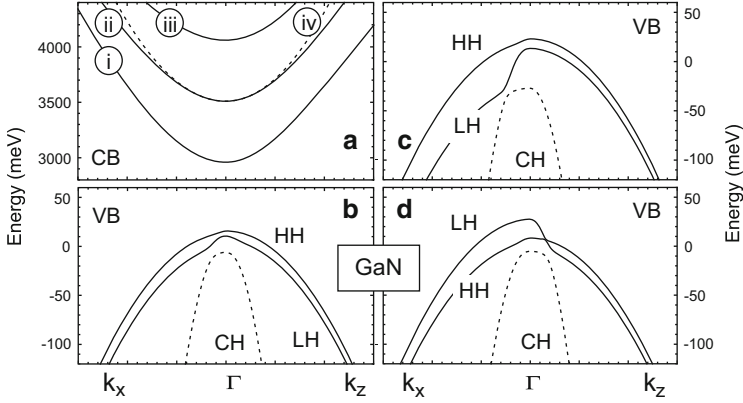


Fig. 2.9 Eight-band $\mathbf{k}\cdot\mathbf{p}$ bandstructure for GaN in presence of (a,i) tensile hydrostatic strain, (a,ii) no strain, (a,iii) compressive hydrostatic strain. (a,iv) No strain and no CB-VB coupling is present. (b) The conduction band is shown in absence of strain, whereas (c) refers to compressive biaxial strain, where the HH-LH splitting is enhanced, and (d) to tensile biaxial strain, finding a reversed HH-LH ordering, with the LH on top. Material parameters are taken from [57]

In the presence of biaxial strain the splitting is enhanced (compressive) (Fig. 2.9c) or reversed (tensile) (Fig. 2.9d).

2.2.5 Energies of Interacting Particles

Due to the resemblance of quantum dot properties to those of atoms, Coulomb interaction is best modeled using methods first developed in quantum chemistry. One of these methods which accounts for the complete spectrum of Coulomb effects, such as direct Coulomb interaction, exchange, and correlation, is the configuration interaction method [15, 16, 47, 64, 70, 79]. Its description, though, is clearly beyond the scope of this contribution. However, in the context of type-II excitons (see Sect. 2.3.2), at least selfconsistent direct Coulomb interaction is required to understand the binding nature of the spatially indirect exciton, which is shortly described in the following.

A self-consistent excitonic cycle consists of repeated calculations of one charge carrier affected not only by the pristine confinement potential but also by the Coulomb attraction of the other carrier, until convergence is reached.

The required Coulomb potential is calculated using the Poisson equation:

$$q_j |\Psi_0^j|^2 = \epsilon_0 \nabla \cdot (\epsilon_s \nabla V_0^j), \quad (2.4)$$

taking into account image charge effects due to the spatial dependence of the dielectric constant, ϵ_s . The index j refers to either the electron or the hole groundstate, Ψ_0^j is the respective wavefunction and V_0^j the arising potential.

For GaN/AlN quantum dots, self-consistency effects are not as important as in the above treated case of type-II excitons. In Sect. 2.3.3.3 we report direct Coulomb energies, which are calculated using the Integral

$$J^{eh} = q_e \int d\mathbf{r} |\Psi_0^e|^2 V_0^h. \quad (2.5)$$

2.3 Discussion of Selected Topics

2.3.1 Zb(001) Versus zb(111) Substrate Orientation

The current interest in the (111)-substrate orientation results from the—compared to (001) substrates—higher surface symmetry [(001): twofold symmetry axis vs (111): threefold symmetry axis, see Fig. 2.10], which is expected to be carried over to the corresponding QD-symmetry.

A more fundamental interest in (111)-QDs stems from the fact that those QDs share properties inherited both from the zinc blende and the wurtzite lattice, since the [111] growth direction possesses many similarities to the *c*-axis of the wurtzite lattice. We refer to the work of Schulz and coworker [66] who published a comprehensive comparison of elastomechanic and piezoelectric properties between the zb-(001), zb-(111), and the wz-*c*-plane based nanostructures.

2.3.1.1 Orientation of the Piezoelectric Field

The major difference between QDs grown on either (001)- or (111)-substrate is the orientation of the piezoelectric field. As it decisively impacts the symmetry properties of the ensuing electronic states a closer inspection is carried out here.

The piezoelectric field and its orientation for (111) grown QDs is of large interest (i) first in view of its impact on the *lateral* symmetry of the confinement potential, and (ii) second with respect to the field distribution in *vertical* direction, the corresponding electron-hole alignment and the related few-particle binding energies.

- (i) To compare the impact of the substrate orientation on the piezoelectric potential (Fig. 2.11) lens-shaped QDs are chosen as model system: for the (111) grown QDs, the potential shows C_{3v} -symmetry and a strong gradient along the growth direction, in contrast to the (001) grown counterpart, with only C_{2v} in-plane symmetry and no significant potential drop along the [001] axis. The field distribution of the (111) grown QD is similar to the one of *c*-plane wurtzite-type GaN/AlN or InN/GaN QDs [5, 53, 81]. The magnitude of the potential drop is much smaller as compared to nitride QDs, where the field additionally depends on pyroelectric effects, which do not occur in zinc blende crystals.

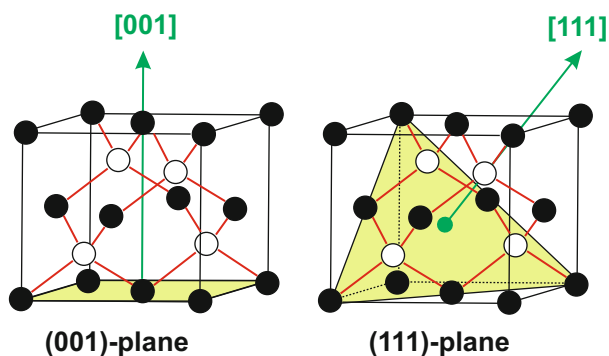


Fig. 2.10 Difference between the (001)- and the (111)-plane in the zinc blende crystal

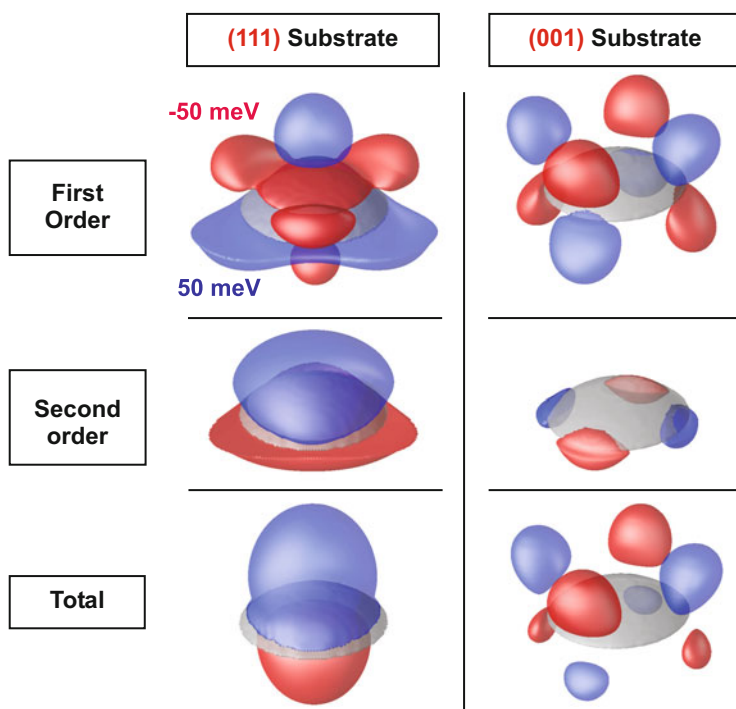


Fig. 2.11 Comparison of the piezoelectric fields (first and second order) for QDs grown on (111)B substrate to those grown on (001). Isosurfaces are shown for values of 50 meV (*blue*) and -50 meV (*red*) respectively. (see [65])

- (ii) The orientation of the piezoelectric field in growth direction results from a subtle interplay between first- and second-order piezoelectric effects. The importance of second-order effects were first discovered for (111)-In(Ga)As/GaAs quantum wells (QW) [10], where the first-order piezoelectric fields alone were found to be not sufficient to explain a number of Stark-shift measurements [19, 20, 33, 60]: For increasing strain the nonlinear piezoelectricity starts to become important. It provides a small but significant contribution to the energy states in quantum wells, because the maximum In concentration in In(Ga)As QWs can hardly exceed $\approx 20\%$ before onset of dislocation generation.

In QDs, much larger In concentrations (up to 100%) can be achieved, which consequently leads to much larger strain inside the QDs. As a result, non-linear piezoelectric effects cannot be neglected in QDs. As can be seen in Fig. 2.11 for (001)-grown InAs QDs (Fig. 2.11 right), first- and second-order effects compensate each other inside the QD [12], whereas in (111)-grown InAs QDs (Fig. 2.11 left and center), the second-order contributions are clearly dominant and therefore determine the orientation of the piezoelectric field.

2.3.1.2 Single Particle States

The first visible differences between the two substrate orientations regarding the electron energy states are the missing electron p -state splitting and a vertical charge separation. The latter further depends on the balance of first- and second order piezoelectric terms for a given composition for (111)-QDs [65]. Energy shifts occur due to different strain field distributions for varying substrate orientation [50].

The excitonic fine-structure splitting in QDs, albeit a two-particle effect, results from a distortion of electron and/or hole groundstate below C_{3v} -symmetry [67]. Such a distortion can originate from QD-elongation, from inequivalent side facets or from piezoelectric fields [67]. The role of the latter is illustrated in Fig. 2.12. For a (001)-grown lens-shaped QD (Fig. 2.12b) the hole groundstate is elongated along [110], whereas in case of a (111)B-grown QD (Fig. 2.12a), electron and hole groundstate show no deformation in any lateral direction.

An important peculiarity of (111)-QDs is the vertical distribution of the piezoelectric field inside the QD and its influence on the vertical position of electron and hole states (Fig. 2.13). In the case of zero piezoelectric field the center of mass of the electron lies above that of the hole [Fig. 2.13(left)]. This is well known from (001)-pyramidal QDs and related to a subtle interplay of the QD shape and strain [69]. Taking into account first-order piezoelectricity enhances the dipole by pulling the hole center of mass down to the QD bottom [Fig. 2.13(middle)]. The electron state moves up less pronounced than the hole state down, because its smaller effective mass makes it more ‘resistant’ against small potential changes. Adding second-order piezoelectric effects, however, reverses the picture completely [Fig. 2.13(right)]. The electron state moves down and the hole state up. Consequently the direction of the dipole changes. In addition, the vertical extension of the hole state increases drastically.

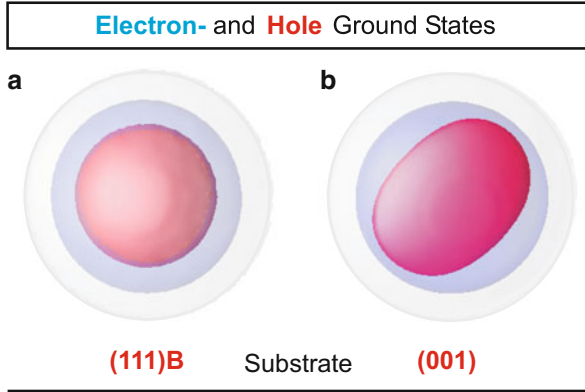


Fig. 2.12 Orientation of electron (*blue*) and hole (*red*) wave function for a lens-shaped QD on two substrate orientations. (see [65])

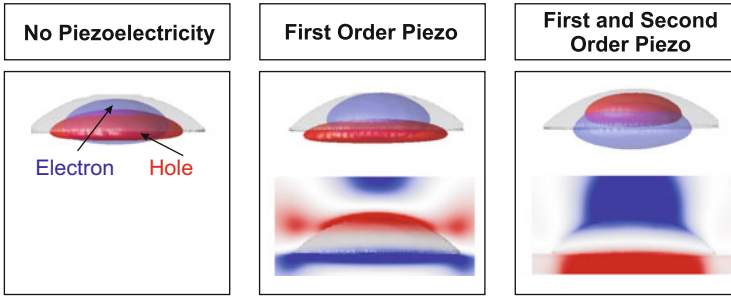


Fig. 2.13 (*upper row*) The position of electron and hole groundstate wavefunction (isosurfaces at 65 % probability density) dependent on the order of the piezoelectric field. (*lower row*) Vertical slices of the piezoelectric potential are shown. (see [65])

2.3.2 Type-I Versus Type-II Confinement

So far we have focused on systems where the band-alignment favors localization of both, electrons and holes. GaSb/GaAs quantum dots by contrast are very particular due to their type-II band alignment. The spatial separation of electrons and holes in type-II structures results in long exciton lifetimes [14, 28, 31, 75], enabling interesting optoelectronic applications [41]. The exclusive confinement of holes and their large localization energy makes GaSb/GaAs QDs particularly interesting for novel charge storage devices [26, 46], called nanoflash memories.

Figure 2.14 compares the local band-edge positions of dimensionally identical, but chemically different QDs: InAs/GaAs (type-I) versus GaSb/GaAs (type-II). The former represents a common anion-system with closely lying valence bands, whereas the latter is a common cation-system with the conduction bands being almost identical (see Fig. 2.14b). Hence, the band-gap difference between GaAs and

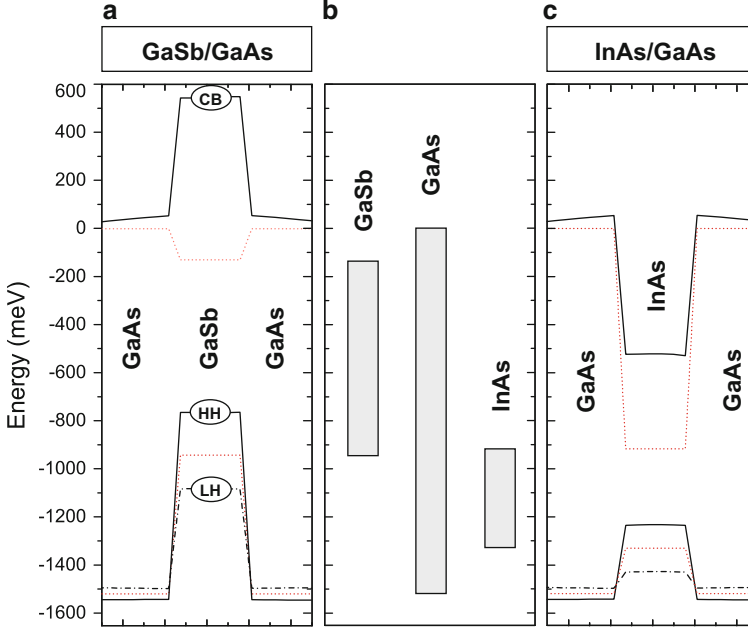


Fig. 2.14 Strained local band edge profiles are shown for quantum dots of same size but different chemical composition: (a) common cation GaSb/GaAs (type-II band alignment), and (c) common anion InAs/GaAs QD (type-I alignment). Part (b), as well as the red dotted lines in (a) and (b), show the band offsets in *absence of strain*

GaSb translates almost completely to a large valence-band offset. In the presence of strain, due to the lattice mismatch, the local band structure of a real heterostructure is strongly modified, leading to a huge increase ($>700\text{ meV}$ for 100 % GaSb content [32]) of the GaSb conduction-band and a clear type-II band alignment (see Fig. 2.14a).

2.3.2.1 Strain Outside the Quantum Dot

If three-dimensional coherent nanostructures are put inside a crystalline matrix of different lattice constant, the resulting strain is not restricted to the inside of the nanostructure, but continues into the surrounding structure. As a result, the local bandstructure is not only altered inside but also outside the quantum dot as can be seen for both systems, InAs/GaAs and GaSb/GaAs, in Fig. 2.14. This finding stands in contrast to ideal quantum wells, where the strain is completely confined inside the layer [29], since the two-dimensional structure is allowed to relax into growth direction.

As the lattice constant of the dots investigated here is bigger than the one of the matrix, the environment is compressively strained, leading to an increase of the local

band edge in the close vicinity of the quantum dot of up to 60 meV. Hence, not only the quantum dot itself acts as repulsive force to electrons in the conduction band but even the close environment, which leads us to the problem of type-II exciton formation.

2.3.2.2 Type-II Exciton Formation

Electrons and holes localized inside the same type-I quantum dot inevitably form excitonic particles, no matter how big the Coulomb attraction is. If, however, the band edge acts repulsive towards one carrier type as in the case of type-II band alignment, exciton- and charged exciton formation is not trivial anymore, but requires additional Coulomb forces to at least form a spatially indirect composite particle.

In the case of GaSb/GaAs quantum dots, the Coulomb attraction needed is supplied by already captured holes, which create an attractive electrostatic potential around the quantum dot for binding electrons. The number of holes needed to at least compensate the strain induced increase of the band edge near the QD, depends on the composition and the vertical aspect ratio (height versus base length) [32]. In Fig. 2.15 the magnitude and the course of the additional potential caused by localized holes inside the QD and the resulting change of the band edge are shown for a flat binary GaSb/GaAs quantum dot. The flat band condition is reached for two localized hole carriers and for four carriers the potential is sufficient to bind an electron above the QD, as can be seen in Fig. 2.15c. A further increase of the number of positive charge carriers increases the Coulomb attraction and leads to a shrinkage of the electron wavefunction.

2.3.3 GaN/AlN Wurtzite Quantum Dots

Owing to a lattice mismatch of about 2.5 % GaN/AlN QDs grow strain induced in the Stranski–Krastanov growth mode. Their typical size and shape is known with great accuracy. Experimental reports on the structural properties of c-plane GaN QDs (e.g. [22, 34, 36, 62, 78]) seem to agree on the shape of the QDs, a truncated hexagonal pyramid with 30° side facets. The reported heights (h) scatter between 1.3 and 5 nm. The aspect ratios ($h:d$, where d denotes the lateral diameter) in most reports are in the range of 1:5–1:10.

The following section is based on the work of Winkelkemper et al. [82]. A series of quantum dots all having the same vertical aspect ratio of 1:5 with a vertical size ranging between 0.8 and 3.6 nm is considered here. The thickness of the wetting layer is assumed to be $w = 0.2$ nm. This set of model QDs covers the major part of experimentally reported QD structures and yields excitonic transition energies and radiative lifetimes [82, Fig. 5] in good agreement with experimental values [18, 36].

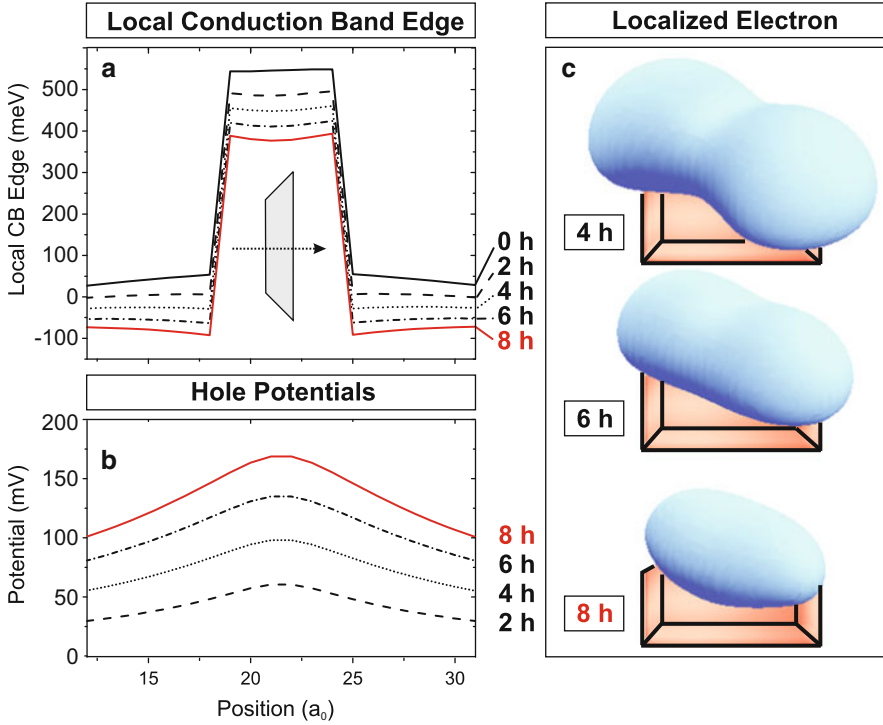


Fig. 2.15 (a) Course of the local conduction band edge as function of prestored hole carriers inside the GaSb/GaAs quantum dot. The QD has a height of about 3 nm and a base length of 22 nm. (b) Calculated electrostatic potential of the differently charged QD: 2 h refers to the occupied hole s-shell, 4 h to additionally occupation of the first p-shell and so on. (c) The first bound electron state is shown for different numbers of occupied hole levels

2.3.3.1 Role of Piezo- and Pyroelectric Built-in Fields

The huge built-in piezo- and pyroelectric fields within GaN/AlN QDs strongly affect the emission energies and radiative lifetimes of localized excitons within the QDs via the quantum-confined Stark effect (QCSE) [5, 17, 18, 78].

Figure 2.16 shows for two QD sizes the course of the piezoelectric and pyroelectric fields (a,b), the resulting local band edges together with the energetic positions of electron and hole groundstate (c,d). The built-in charges generate fields are as large as 8.0 MV/cm in the center of the QD leading to a strong spatial separation of electron and hole states (Fig. 2.17a,b). Depending on the size of the QDs the electron-hole overlap varies strongly, resulting in radiative lifetimes ranging from a few nanoseconds for small QDs up to as long as 100 μ s for large QDs.

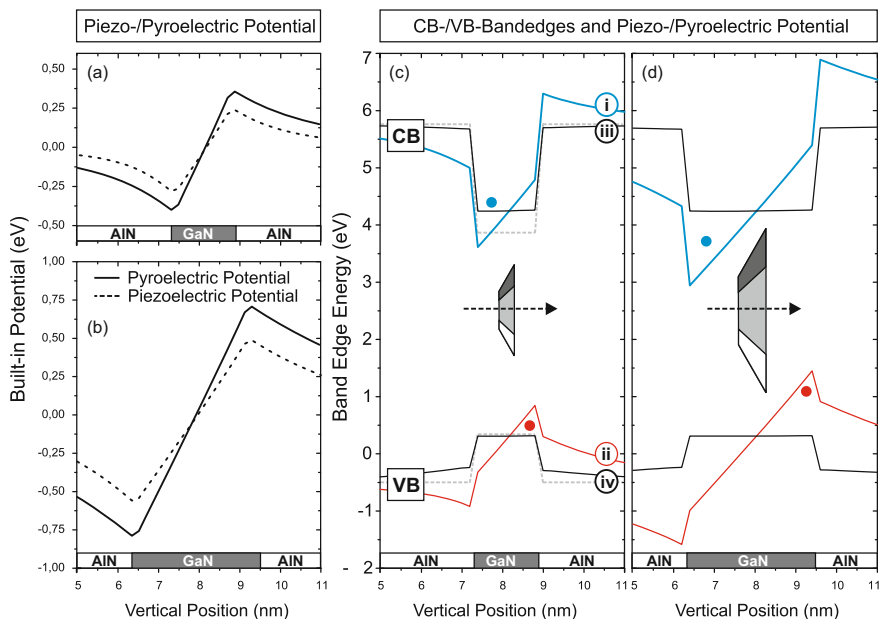


Fig. 2.16 (a,b) Piezo- and pyroelectric potentials ($e\phi$) shown for two QDs of different height: (a) $h=1.6$ nm, (b) $h=3.2$ nm. (c,d) The resulting local band edges are plotted for the cases (i,ii) strain and built-in fields, (iii,iv) strain but no built-in field, and gray, dotted: neither strain, nor piezo- and pyroelectric built-in field. The blue and red dots indicate the energetic and spatial position of the electron and hole groundstates

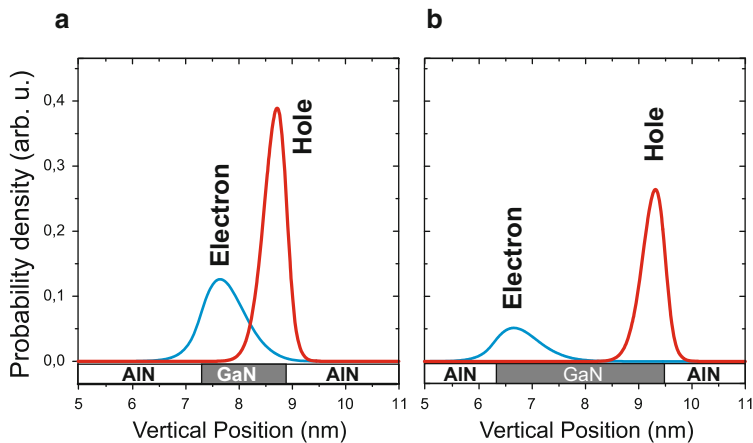


Fig. 2.17 (a,b) Probability density of electron and hole groundstate as function of QD-height

2.3.3.2 Single Particle Energy Levels

The bound hole states in GaN/AlN QDs are formed predominantly by the A- and B-band. C-band contributions are small because the biaxial strain within the QDs shifts this band to much lower energies [81, 83]. As a first approximation, for each band we expect to find a ground state with an s-shaped envelope function, which is only spin degenerate. The p-shell consists of two degenerate states and the d-shell of three. More p- and d-states with nodal planes along the growth direction are expected at much higher energies owing to the strong vertical confinement.

Due to the different parities of the bulk conduction and valence bands, the electron and hole states have a finite optical matrix element, if their envelope functions have the same parity, i.e. the allowed transition channels are s-s, p-p, s-d, etc. Each transition channel exists twice, once for the A-type holes and once for the B-type holes. Figure 2.18 shows the single-particle electron and hole energy levels of all QDs considered in this work including the five energetically lowest (highest) electron (hole) states. The electron states are all formed predominantly by the conduction band ($\approx 95\%$). Therefore, s, p and d shells can be clearly distinguished. The hole spectra, however, are more complex, because hole states are not formed by either the A- or B-band, but by a mixture of both bands and even a small C-band contribution. Still each hole state can be characterized by the band that contributes most to it (see labels in Fig. 2.18). The A-band s-state ($h_0(A)$; $\approx 95\%$ A-band projection) and the B-band s-state ($h_1(B)$; $\approx 90\%$ B-band projection) are energetically well separated from the excited hole states. Both have an unambiguously s-shaped envelope function (not shown here). The splitting between both states ($\approx 9\text{--}10\text{ meV}$) does not increase for smaller QDs, but is constant. It corresponds to the energy separation between A- and B-band in strained GaN. The higher excited hole states cannot be assigned to p- or d-like orbitals. Please note that, although they have been labeled according to the major band contributions, such contribution sometimes does not exceed 50%.

2.3.3.3 Coulomb Interaction

GaN *bulk* excitons are well known for their stability even at room-temperature owing to their large exciton binding energy of 26 meV [58] which makes heterostructures based on GaN promising candidates for the realization of polariton lasers [45]. The question arises how the exciton binding energy is affected by a three-dimensional confinement as in the case of GaN/AlN QDs. Here, to display the major effect, we calculate the electron-hole binding energy, hence, leaving out selfconsistency and correlation effects. As can be seen from Fig. 2.19 height variations and the consequent change in electron-hole separation strongly affects the resulting Coulomb binding strength leading to values ranging from 160 meV for small QDs down to about 40 meV for large QDs being much larger than for GaN bulk.

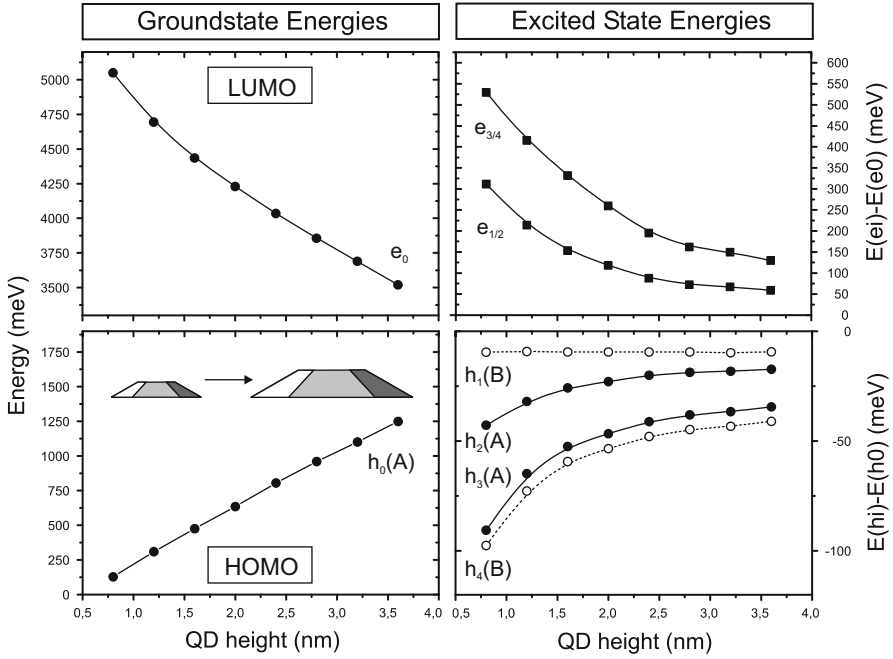


Fig. 2.18 Electron and hole single-particle energies as function of QD size. LUMO (HOMO) refers to the electron (hole) groundstate

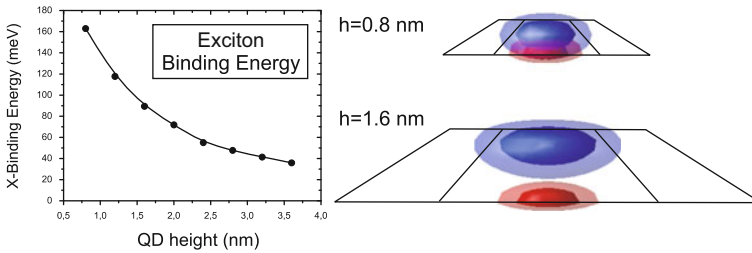


Fig. 2.19 (left) Electron-hole Coulomb binding energy as function of QD size. (right) Electron and hole probability densities are shown for two QDs of different size highlighting the different wavefunction extent and the rising electron-hole distance with increasing QD-height

2.4 Conclusion

In this chapter we gave an overview on the envelope function based eight-band $\mathbf{k}\cdot\mathbf{p}$ method for electronic structure calculations of QDs. Three types of heterostructures of particular current interest are used to exemplify the wide range of applicability of the method. It was shown that the theory is able to seamlessly account for different lattice systems, band-alignments and substrate orientations.

Acknowledgements Many colleagues contributed to the success of this work. However, three people stand out who contributed most over the past 20 years: We feel deeply indebted to Oliver Stier, Momme Winkelnekemper, and Marius Grundmann.

The work was funded by DFG in the frame of SFBs 296 and 787.

References

1. W.G. Cady *Piezoelectricity: an Introduction to the Theory and Applications of Electromechanical Phenomena in Crystals* (McGraw-Hill, 1946)
2. O. Ambacher, M. Eickhoff, A. Link, M. Hermann, M. Stutzmann, F. Bernardini, V. Fiorentini, Y. Smorchkova, J. Speck, U. Mishra, W. Schaff, V. Tilak, L.F. Eastman, Electronics and sensors based on pyroelectric AlGaIn/GaN heterostructures. *Phys. Stat. Sol. (c)* **0**(6), 1878–1907 (2003)
3. O. Ambacher, J. Majewski, C. Miskys, A. Link, M. Hermann, M. Eickhoff, M. Stutzmann, F. Bernardini, V. Fiorentini, V. Tilak, Pyroelectric properties of Al (In) GaN/GaN hetero- and quantum well structures. *J. Phys.: Condens. Matter* **14**(13), 3399 (2002)
4. A.D. Andreev, E.P. O'Reilly, Theory of the electronic structure of GaN/AlN hexagonal quantum dots. *Phys. Rev. B* **62**(23), 851–870 (2000)
5. A.D. Andreev, E.P. O'Reilly, Optical transitions and radiative lifetime in GaN/AlN self-organized quantum dots. *Appl. Phys. Lett.* **79**(4), 521 (2001)
6. N. Baer, S. Schulz, P. Gartner, S. Schumacher, G. Czycholl, F. Jahnke, Influence of symmetry and Coulomb correlation effects on the optical properties of nitride quantum dots. *Phys. Rev. B* **76**(7) (2007)
7. N. Baer, S. Schulz, S. Schumacher, P. Gartner, G. Czycholl, F. Jahnke, Optical properties of self-organized wurtzite InN/GaN quantum dots: A combined atomistic tight-binding and full configuration interaction calculation. *Appl. Phys. Lett.* **87**(23), 114–231 (2005)
8. T. Bahder, Eight-band $\mathbf{k}\cdot\mathbf{p}$ model of strained zinc-blende crystals. *Phys. Rev. B* **41**(17), 992–1012 (1990)
9. F. Bernardini, V. Fiorentini, D. Vanderbilt, Spontaneous polarization and piezoelectric constants of III-V nitrides. *Phys. Rev. B* **56**(16), 10,024–10,027 (1997)
10. G. Bester, X. Wu, D. Vanderbilt, A. Zunger, Importance of second-order piezoelectric effects in zinc-blende semiconductors. *Phys. Rev. Lett.* **96**(18) (2006)
11. G. Bester, A. Zunger, Cylindrically shaped zinc-blende semiconductor quantum dots do not have cylindrical symmetry: Atomistic symmetry, atomic relaxation, and piezoelectric effects. *Phys. Rev. B* **71**(4) (2005)
12. G. Bester, A. Zunger, X. Wu, D. Vanderbilt, Effects of linear and nonlinear piezoelectricity on the electronic properties of InAs/GaAs quantum dots. *Phys. Rev. B* **74**(8) (2006)
13. D. Bimberg, M. Grundmann, N.N. Ledentsov, *Quantum Dot Heterostructures* (John Wiley & Sons, New York, 1999)
14. H. Born, L. Müller-Kirsch, R. Heitz, A. Hoffmann, D. Bimberg, Rapid research notes-radiative recombination in type II GaSb/GaAs quantum dots. *Phys. Stat. Sol. (b)* **228**(3), 4 (2001)
15. M. Braskén, M. Lindberg, D. Sundholm, J. Olsen, Full configuration interaction calculations of electron-hole correlation effects in strain-induced quantum dots. *Phys. Rev. B* **61**(11), 7652–7655 (2000)
16. M. Braskén, M. Lindberg, D. Sundholm, J. Olsen, Full configuration interaction calculations of electron-hole correlation effects in strain-induced quantum dots. *Phys. Stat. Sol. (b)* **224**(3), 775–779 (2001)
17. T. Bretagnon, S. Kalliakos, P. Lefebvre, P. Valvin, B. Gil, N. Grandjean, A. Dussaigne, B. Damilano, J. Massies, Time dependence of the photoluminescence of GaN/AlN quantum dots under high photoexcitation. *Phys. Rev. B* **68**(20), 205–301 (2003)

18. T. Bretagnon, P. Lefebvre, P. Valvin, R. Bardoux, T. Guillet, T. Taliercio, B. Gil, N. Grandjean, F. Semond, B. Damlano, A. Dussaigne, J. Massies, Radiative lifetime of a single electron-hole pair in GaN/AlN quantum dots. *Phys. Rev. B* **73**(11), 113–304 (2006)
19. C.H. Chan, M.C. Chen, H.H. Lin, Y.F. Chen, G.J. Jan, Y.H. Chen, Characterization of piezoelectric (111)B InGaAs/GaAs p-i-n quantum well structures using photoreflectance spectroscopy. *Appl. Phys. Lett.* **72**(10), 1208 (1998)
20. S. Cho, J. Kim, A. Sanz-Hervás, A. Majerfeld, G. Patriarche, B.W. Kim, Characterization of piezoelectric and pyroelectric properties of MOVPE-grown strained (111)A InGaAs/GaAs QW structures by modulation spectroscopy. *Phys. Stat. Sol. (a)* **195**(1), 260–264 (2003)
21. M. Cusack, P. Briddon, Electronic structure of InAs/GaAs self-assembled quantum dots. *Phys. Rev. B* (1996)
22. B. Daudin, F. Widmann, G. Feuillet, Y. Samson, M. Arlery, J. Rouvière, Stranski-Krastanov growth mode during the molecular beam epitaxy of highly strained GaN. *Phys. Rev. B* **56**(12), R7069–R7072 (1997)
23. P. Enders, A. Bärwolff, M. Woerner, D. Suisky, **k·p** theory of energy bands, wave functions, and optical selection rules in strained tetrahedral semiconductors. *Phys. Rev. B* **51**(23), 16,695–16,704 (1995)
24. V.A. Fonoberov, A.A. Balandin, Excitonic properties of strained wurtzite and zinc-blende GaN/Al_{1-x}Ga_xN quantum dots. *J. Appl. Phys.* **94**(11), 7178 (2003)
25. H. Fu, L.W. Wang, A. Zunger, Applicability of the **k·p** method to the electronic structure of quantum dots. *Phys. Rev. B* **57**(16), 9971–9987 (1998)
26. M. Geller, A. Marent, T. Nowozin, D. Bimberg, N. Akçay, N. Öncan, A write time of 6 ns for quantum dot-based memory structures. *Appl. Phys. Lett.* **92**(9), 092–108 (2008)
27. D. Gershoni, C.H. Henry, G.A. Baraff, Calculating the optical properties of multidimensional heterostructures: Application to the modeling of quaternary quantum well lasers. *IEEE J. Quantum Electron.* **29**(9), 2433–2450 (1993)
28. K. Gradkowski, T.J. Ochalski, D.P. Williams, J. Tatebayashi, A. Khoshakhlagh, G. Balakrishnan, E.P. O'Reilly, G. Huyet, L.R. Dawson, D.L. Huffaker, Optical transition pathways in type-II Ga(As)Sb quantum dots. *J. Luminescence* **129**(5), 456–460 (2009)
29. M. Grundmann, O. Stier, D. Bimberg, InAs/GaAs pyramidal quantum dots: Strain distribution, optical phonons, and electronic structure. *Phys. Rev. B* **52**(16), 11,969 (1995)
30. T. Hammerschmidt, Role of strain relaxation during different stages of InAs quantum dot growth. In: *Physics of Semiconductors: 27th International Conference on the Physics of Semiconductors - ICPS-27*, pp. 601–602. AIP (2005)
31. F. Hatami, M. Grundmann, N. Ledentsov, F. Heinrichsdorff, R. Heitz, J. Böhrer, D. Bimberg, S. Ruvimov, P. Werner, V. Ustinov, P. Kop'ev, Z. Alferov, Carrier dynamics in type-II GaSb/GaAs quantum dots. *Phys. Rev. B* **57**(8), 4635–4641 (1998)
32. M. Hayne, J. Maes, S. Bersier, V.V. Moshchalkov, A. Schliwa, L. Müller-Kirsch, C. Kapteyn, R. Heitz, D. Bimberg, Electron localization by self-assembled GaSb/GaAs quantum dots. *Appl. Phys. Lett.* **82**(24), 4355–4357 (2003)
33. R. Hogg, T. Fisher, A. Willcox, D. Whittaker, M. Skolnick, D. Mowbray, J. David, A. Pabla, G. Rees, R. Grey, J. Woodhead, J. Sanchez-Rojas, G. Hill, M. Pate, P. Robson, Piezoelectric-field effects on transition energies, oscillator strengths, and level widths in (111)B-grown (In,Ga)As/GaAs multiple quantum wells. *Phys. Rev. B* **48**(11), 8491–8494 (1993)
34. K. Hoshino, S. Kako, Y. Arakawa, Formation and optical properties of stacked GaN self-assembled quantum dots grown by metalorganic chemical vapor deposition. *Appl. Phys. Lett.* **85**(7), 1262–1264 (2004)
35. H. Jiang, J. Singh, Strain distribution and electronic spectra of InAs/GaAs self-assembled dots: An eight-band study. *Phys. Rev. B* **56**(8), 4696–4701 (1997)
36. S. Kako, C. Santori, K. Hoshino, S. Götzinger, Y. Yamamoto, Y. Arakawa, A gallium nitride single-photon source operating at 200K. *Nat Mater* **5**(11), 887–892 (2006)
37. E. Kane, *Energy Band Theory* (Handbook on Semiconductors, 1982)

38. E.Kane, Phonon spectra of diamond and zinc-blende semiconductors. *Phys. Rev. B* **31**(12), 7865–7876 (1985)
39. J. Kim, L.W. Wang, A. Zunger, Comparison of the electronic structure of InAs/GaAs pyramidal quantum dots with different facet orientations. *Phys. Rev. B* **57**(16), R9408–R9411 (1998)
40. N. Kirstaedter, N.N. Ledentsov, M. Grundmann, D. Bimberg, V.M. Ustinov, S.S. Ruvimov, M.V. Maximov, P.S. Kop'ev, Z.I. Alferov, U. Richter, P. Werner, U. Gosele, J. Heydenreich, Low threshold, large To injection laser emission from (InGa)As quantum dots. *Electron. Lett.* **30**(17), 1416–1417 (1994)
41. R.B. Laghumavarapu, A. Moscho, A. Khoshakhlagh, M. El-Emawy, L.F. Lester, D.L. Huffaker, GaSb/GaAs type II quantum dot solar cells for enhanced infrared spectral response. *Appl. Phys. Lett.* **90**(17), 173,125–173,125–3 (2007)
42. O.L. Lazarenkova, P. von Allmen, F. Oyafo, S. Lee, G. Klimeck, Effect of anharmonicity of the strain energy on band offsets in semiconductor nanostructures. *Appl. Phys. Lett.* **85**(18), 4193 (2004)
43. S. Lee, F. Oyafo, P. von Allmen, G. Klimeck, Boundary conditions for the electronic structure of finite-extent embedded semiconductor nanostructures. *Phys. Rev. B* **69**(4), 045,316 (2004)
44. J.A. Majewski, S. Birner, A. Trellakis, M. Sabathil, P. Vogl, Advances in the theory of electronic structure of semiconductors. *Phys. Stat. Sol. (c)* **1**(8), 2003–2027 (2004)
45. G. Malpuech, A. Di Carlo, A. Kavokin, J.J. Baumberg, M. Zamfirescu, P. Lugli, Room-temperature polariton lasers based on GaN microcavities. *Appl. Phys. Lett.* **81**(3), 412–414 (2002)
46. A. Marent, M. Geller, A. Schliwa, D. Feise, K. Pötschke, D. Bimberg, N. Akçay, N. Öncan, 10^6 years extrapolated hole storage time in GaSb/AlAs quantum dots. *Appl. Phys. Lett.* **91**(24), 242,109 (2007)
47. R. McWeeny, B.T. Pickup, Quantum theory of molecular electronic structure. *Rep. Prog. Phys.* **43**(9), 1065–1144 (2000)
48. P. Michler, A quantum dot single-photon turnstile device. *Science* **290**(5500), 2282–2285 (2000)
49. M. Migliorato, A. Cullis, M. Fearn, J. Jefferson, Atomistic simulation of strain relaxation in $\text{In}_x\text{Ga}_{1-x}\text{As/GaAs}$ quantum dots with nonuniform composition. *Phys. Rev. B* **65**(11), 115,316 (2002)
50. V. Mlinar, F.M. Peeters, Optical properties of (In,Ga)As capped InAs quantum dots grown on [11k] substrates. *Appl. Phys. Lett.* **91**(2), 021,910 (2007)
51. V. Mlinar, A. Zunger, Spectral barcoding of quantum dots: deciphering structural motifs from the excitonic spectra. *Phys. Rev. B* **80**(3), 035,328 (2009)
52. F.H. Pollak, Effects of homogeneous strain on the electronic and vibrational levels in semiconductors. In: T.P. Pearsall (ed.) *Semiconductors and Semimetals*, p. 17. Strained-Layer Superlattices: Physics (1990)
53. M. Povolotskyi, A. Di Carlo, S. Birner, Electronic and optical properties of [N11] grown nanostructures. *Phys. Stat. Sol. (c)* **1**(6), 1511–1521 (2004)
54. C. Pryor, Eight-band calculations of strained InAs/GaAs quantum dots compared with one-, four-, and six-band approximations. *Phys. Rev. B* **57**(12), 7190–7195 (1998)
55. C. Pryor, J. Kim, L.W. Wang, A.J. Williamson, A. Zunger, Comparison of two methods for describing the strain profiles in quantum dots. *J. Appl. Phys.* **83**(5), 2548 (1998)
56. V. Ranjan, G. Allan, C. Priester, C. Delerue, Self-consistent calculations of the optical properties of GaN quantum dots. *Phys. Rev. B* **68**(11) (2003)
57. P. Rinke, M. Scheffler, A. Qteish, M. Winkelnkemper, D. Bimberg, J. Neugebauer, Band gap and band parameters of InN and GaN from quasiparticle energy calculations based on exact-exchange density-functional theory. *Appl. Phys. Lett.* **89**(16), 161,919 (2006)
58. A. Rodina, M. Dietrich, A. Göldner, L. Eckey, A. Hoffmann, A. Efros, M. Rosen, B. Meyer, Free excitons in wurtzite GaN. *Phys. Rev. B* **64**(11), 115,204 (2001)
59. T. Saito, Y. Arakawa, Electronic structure of piezoelectric $\text{In}_{0.2}\text{Ga}_{0.8}\text{N}$ quantum dots in GaN calculated using a tight-binding method. *Physica E* **15**(3), 169–181 (2002)

60. J.L. Sanchez Rojas, A. Sacedon, F. Gonzalez Sanz, E. Calleja, E. Munoz, Dependence on the In concentration of the piezoelectric field in (111)B InGaAs/GaAs strained heterostructures. *Appl. Phys. Lett.* **65**(16), 2042–2044 (1994)
61. R. Santoprete, B. Koiller, R. Capaz, P. Kratzer, Q. Liu, M. Scheffler, Tight-binding study of the influence of the strain on the electronic properties of InAs/GaAs quantum dots. *Phys. Rev. B* **68**(23) (2003)
62. C. Santori, S. Götzinger, Y. Yamamoto, S. Kako, K. Hoshino, Y. Arakawa, Photon correlation studies of single GaN quantum dots. *Appl. Phys. Lett.* **87**(5), 051,916–051,916–3 (2005)
63. A. Schliwa, M. Winkelnkemper, D. Bimberg, Impact of size, shape, and composition on piezoelectric effects and electronic properties of In(Ga)As/GaAs quantum dots. *Phys. Rev. B* **76**(20) (2007)
64. A. Schliwa, M. Winkelnkemper, D. Bimberg, Few-particle energies versus geometry and composition of $\text{In}_x\text{Ga}_{1-x}\text{As}/\text{GaAs}$ self-organized quantum dots. *Phys. Rev. B* **79**(7) (2009)
65. A. Schliwa, M. Winkelnkemper, A. Lochmann, E. Stock, D. Bimberg, In(Ga)As/GaAs quantum dots grown on a (111) surface as ideal sources of entangled photon pairs. *Phys. Rev. B* **80**(16) (2009)
66. S. Schulz, M.A. Caro, E.P. O'Reilly, O. Marquardt, Symmetry-adapted calculations of strain and polarization fields in (111)-oriented zinc-blende quantum dots. *Phys. Rev. B* **84**(12), 125,312 (2011)
67. R. Seguin, A. Schliwa, S. Rodt, K. Pötschke, U. Pohl, D. Bimberg, Size-dependent fine-structure splitting in self-organized InAs/GaAs quantum dots. *Phys. Rev. Lett.* **95**(25) (2005)
68. V. Shchukin, D. Bimberg, Spontaneous ordering of nanostructures on crystal surfaces. *Rev. Mod. Phys.* **71**(4), 1125–1171 (1999)
69. W. Sheng, J.P. Leburton, Electron-hole alignment in InAs/GaAs self-assembled quantum dots: effects of chemical composition and dot shape. *Phys. Rev. B* **63**(16) (2001)
70. E. Siebert, T. Warming, A. Schliwa, E. Stock, M. Winkelnkemper, S. Rodt, D. Bimberg, Spectroscopic access to single-hole energies in InAs/GaAs quantum dots. *Phys. Rev. B* **79**(20) (2009)
71. R. Singh, G. Bester, Nanowire quantum dots as an ideal source of entangled photon pairs. *Phys. Rev. Lett.* **103**(6) (2009)
72. J.C. Slater, G.F. Koster, Simplified LCAO method for the periodic potential problem. *Phys. Rev.* **94**(6), 1498–1524 (1954)
73. O. Stier, D. Bimberg, Modeling of strained quantum wires using eight-band $\mathbf{k}\cdot\mathbf{p}$ theory. *Phys. Rev. B* **55**(12), 7726–7732 (1997)
74. O. Stier, M. Grundmann, D. Bimberg, Electronic and optical properties of strained quantum dots modeled by 8-band $\mathbf{k}\cdot\mathbf{p}$ theory. *Phys. Rev. B* **59**(8), 5688 (1999)
75. C.K. Sun, G. Wang, J.E. Bowers, B. Brar, H.R. Blank, H. Kroemer, M.H. Pilkuhn, Optical investigations of the dynamic behavior of GaSb/GaAs quantum dots. *Appl. Phys. Lett.* **68**(11), 1543–1545 (1996)
76. J. Tersoff, Modeling solid-state chemistry: interatomic potentials for multicomponent systems. *Phys. Rev. B* **39**(8), 5566–5568 (1989)
77. I. Vurgaftman, J.R. Meyer, Band parameters for nitrogen-containing semiconductors. *J. Appl. Phys.* **94**(6), 3675 (2003)
78. F. Widmann, J. Simon, B. Daudin, G. Feuillet, J. Rouvière, N. Pelekanos, G. Fishman, Blue-light emission from GaN self-assembled quantum dots due to giant piezoelectric effect. *Phys. Rev. B* **58**(24), R15,989–R15,992 (1998)
79. A.J. Williamson, A. Franceschetti, A. Zunger, Multi-excitons in self-assembled InAs/GaAs quantum dots: a pseudopotential, many-body approach. *Europhys. Lett.* **53**(1), 59–65 (2007)
80. A.J. Williamson, L. Wang, A. Zunger, Theoretical interpretation of the experimental electronic structure of lens-shaped self-assembled InAs/GaAs quantum dots. *Phys. Rev. B* **62**(19), 12,963–12,977 (2000)
81. M. Winkelnkemper, A. Schliwa, D. Bimberg, Interrelation of structural and electronic properties in $\text{In}_x\text{Ga}_{1-x}\text{N}/\text{GaN}$ quantum dots using an eight-band $\mathbf{k}\cdot\mathbf{p}$ model. *Phys. Rev. B* **74**(15) (2006)

82. M. Winkelkemper, R. Seguin, S. Rodt, A. Hoffmann, D. Bimberg, GaN/AlN quantum dots for single qubit emitters. *J. Phys.: Condens. Matter* **20**(45), 454,211 (2008)
83. M. Winkelkemper, R. Seguin, S. Rodt, A. Schliwa, L. Reissmann, A. Strittmatter, A. Hoffmann, D. Bimberg, Polarized emission lines from A- and B-type excitonic complexes in single InGaN/GaN quantum dots. *J. Appl. Phys.* **101**(11), – (2007)

Multi-Band Effective Mass Approximations
Advanced Mathematical Models and Numerical
Techniques

Ehrhardt, M.; Koprucki, Th. (Eds.)

2014, XVI, 318 p. 83 illus., 62 illus. in color., Hardcover

ISBN: 978-3-319-01426-5